Elastic full-waveform inversion of seismic ambient noise

Ludovic Métivier[1,2], Grégory Bièvre[2], Romain Brossier[2], Jian Cao[2,3], Stéphane Garambois[2], Ahmed Nouibat[4], Giuseppe Provenzano[2], and Alizia Tarayoun[2]

https://doi.org/10.1190/tle44050373a1.1

Abstract

Elastic full-waveform inversion (FWI) is appealing for an enhanced integration of wave physics propagation and the resulting improved characterization of the subsurface due to the reconstruction of P- and S-wave velocity models. While the high computational cost of elastic FWI can be controlled using adequate numerical methods, the increase in the nonlinearity of elastic FWI calls for dedicated strategies to design initial P- and S-wave velocity models and access low-frequency data. We believe that the recent surge in ocean-bottom sensor acquisition is an opportunity to develop such strategies. The seismic ambient noise recorded by an array of receivers can be stacked to reconstruct interstation Green's functions that can be further used as low-frequency input data for elastic FWI to generate low-resolution P- and S-wave velocity models. We illustrate two applications of this strategy at two different scales: the first for near-surface imaging in a landslide context, the second for the reconstruction of a high-resolution S-wave velocity model at the Alps scale. In both cases, the seismic ambient noise Green's functions are efficiently matched, and accurate velocity models are built.

Introduction

Full-waveform inversion (FWI) is a seismic imaging method introduced by Lailly (1983) and Tarantola (1984), based on the quantitative fit of the full seismic data (amplitudes and phases) through an iterative least-squares process. At each iteration, synthetic data are computed through the solution of partial differential equations describing the propagation of mechanical waves within the imaged region. Compared with conventional seismic imaging processing, based on traveltime tomography for the reconstruction of a smooth velocity model followed by migration for the reconstruction of a high-resolution reflectivity image, FWI results in broadband improved reconstructions of subsurface models that best predict the seismic observed data using a given wave propagation engine.

The first application of FWI to 3D field data at the exploration scale was performed by Sirgue et al. (2010), who present a high-resolution reconstruction of the P-wave velocity model of the Valhall Field in the Norwegian sector of the North Sea. Since then, industry interest in FWI has constantly increased, as witnessed by the number of FWI applications in the past 15 years.

FWI today is a central piece of the seismic imaging workflow, providing high-resolution reconstruction of subsurface parameters (mainly seismic wave velocities). A current trend in the industry is to improve the accuracy of the physics of wave propagation within FWI algorithms. Most 3D FWI applications, especially from marine data, currently are performed within the acoustic approximation. However, recent work illustrates the limitations of this approach, even using marine data, in the presence of highly contrasting geologic units such as salt bodies (Rivera et al., 2019). In this case, the amplitude variation with offset (AVO) response is not predicted correctly, resulting in incorrect salt body geometries and poor subsalt imaging. Using an elastic approximation, it is possible to correct the P-wave velocity estimation from these artifacts. To a larger extent, elastic FWI is promising because it makes it possible to build high-resolution quantitative models of both P- and S-wave velocities simultaneously. Such a two-model characterization carries much more information on the subsurface mechanical state, especially regarding its fluid content, than a single P-wave velocity model. This allows downscaling approaches to recover microparameters such as porosity or saturation, toward reservoir characterization. This is an especially interesting perspective for reservoir and gas storage monitoring, a problem put forward by the current development of carbon capture and storage facilities.

Developing 3D elastic FWI methods, however, raises several challenges. The most obvious might be the increased computational cost: the computational complexity for evaluating numerical solutions of elastic wave equations reaches two orders of magnitude higher than in the acoustic case. Another important aspect is the need to accurately model interface waves: Rayleigh and Love waves in land configuration, Scholte waves in marine configuration. These waves are dominant in the elastic response of the subsurface, and conventional finite-difference techniques have been shown to struggle to model them accurately in the presence of varying topography or bathymetry. Finally, a significant challenge for elastic FWI is the increased nonlinearity of the elastic inverse problem compared with the acoustic case. Beyond designing more robust schemes, a fundamental question is how to recover sufficiently low frequency data and to design sufficiently accurate initial models, both for P- and S-wave velocities.

While overcoming the first two difficulties relies on the design of dedicated numerical schemes, a solution to the nonlinearity

Manuscript received 18 December 2024; accepted 10 February 2025.
[1]Université Grenoble Alpes, CNRS, LJK, F-38000 Grenoble, France. E-mail: ludovic.metivier@univ-grenoble-alpes.fr.
[2]Université Grenoble Alpes, ISTerre, F-38000 Grenoble, France. E-mail: gregory.bievre@univ-grenoble-alpes.fr; romain.brossier@univ-grenoble-alpes.fr; stephane.garambois@univ-grenoble-alpes.fr; geo.giuseppeprovenzano@gmail.com; alizia.tarayoun@univ-grenoble-alpes.fr.
[3]Now at Viridien, Massy, France. E-mail: jian.cao@viridiengroup.com.
[4]University of Strasbourg, CNRS, Institut Terre et Environnement de Strasbourg, UMR 7063, F-67084 Strasbourg, France. E-mail: nouibat@unistra.fr.

difficulty might rely on deployment of permanent or temporary sensors, a practice that has increased significantly in recent years. For FWI with marine data, for instance in the Gulf of Mexico, the deployment of ocean-bottom sensors (OBS) has been shown to be especially valuable because the decoupling between the sources and receivers makes it possible to record long-offset/wide-azimuth data, provided a sufficiently energetic source can be used. This makes it possible to record diving waves with increased penetration depth, which can be efficiently exploited by conventional FWI to provide deep high-resolution velocity models. (See Merritt et al., 2024, for a recent example of subsalt imaging in the Gulf of Mexico.)

The deployment of continuously recording seismic stations makes it possible to record the seismic ambient noise. The cross-correlation stack of ambient noise recorded by two stations can converge, under specific assumptions, toward the interstation impulse response. This result, which has its roots in exploration seismic (Claerbout, 1968), acoustic physics (Lobkis and Weaver, 2001), and seismology (Aki, 1957), could be crucial for future elastic FWI applications. The virtual, interferometry data, built from ambient noise, can be inverted using elastic FWI. As it is mostly driven by low-frequency surface waves, this yields an effective way to produce accurate initial P- and S-wave velocity models. An example of reconstruction of a shallow S-velocity model from ambient noise tomography is presented for instance in Mordret et al. (2013), using ocean-bottom cable (OBC) data deployed at the Valhall Field in the Norwegian North Sea.

This study presents two applications of elastic FWI to interferometry data at different scales. The first application is at the near-surface scale, in a land configuration, for the imaging of a landslide zone in the southeast of France at Harmalière. The use of passive data in this case is key to preserving the integrity of a potentially unstable investigation zone. The second is a regional-scale application for imaging the western Alps and the Ligurian-Provence back-arc basin. In this case, a network of permanent and temporary stations, some of which are deployed in the Ligurian Sea, are used to build the interferometry data set. The presence of stations in the water necessitates the use of a fluid-solid-coupled modeling engine. We reconstruct a high-resolution S-wave velocity model in the Alps region from which a high-resolution Moho map is deduced. Both applications rely on SEM46, a viscoelastic full-waveform modeling and inversion software developed in the SEISCOPE project, which we briefly present in the following.

Methods

Viscoelastic FWI with fluid-solid coupling and spectral element discretization. We consider the following viscoelastic wave propagation equations, relying on standard linear solid (SLS) mechanisms to model the attenuation (Carcione et al., 1988):

$$\begin{cases} \rho \partial_{tt}\mathbf{u} + \mathbf{DCD}^T\mathbf{u} + \mathbf{DC}^a \sum_{l=1}^{L} \Psi_l = \mathbf{f}, \\ \partial_t \Psi_l + \omega_l \Psi_l - y_l \omega_l \mathbf{D}^T\mathbf{u} = 0, \end{cases} \tag{1}$$

where $\mathbf{u}(\mathbf{x},t)$ is the particle displacement, $\mathbf{f}$ is a force source term, ρ is the density, $\mathbf{C}$ is the stiffness tensor represented as a six-by-six matrix following Voigt notations, $\mathbf{C}^a$ is the relaxed stiffness tensor, such that

$$\mathbf{C}^a_{IJ} = Q^{-1}_{IJ}\mathbf{C}_{IJ}, \; I = 1, \ldots, 6, \quad J = 1, \ldots, 6, \tag{2}$$

where Q_{IJ} is a quality factor representing the attenuation, $\mathbf{D}$ is the matrix of spatial derivatives,

$$\mathrm{D} = \begin{pmatrix} \partial x_1 & 0 & 0 & 0 & \partial x_3 & \partial x_2 \\ 0 & \partial x_2 & 0 & \partial x_3 & 0 & \partial x_1 \\ 0 & 0 & \partial x_3 & \partial x_2 & \partial x_1 & 0 \end{pmatrix}, \tag{3}$$

and Ψ_l are the SLS relaxation mechanisms representing the attenuation with reference frequency ω_l, while y_l are scalar parameters tuned to fit specific frequency dependence laws for the quality factors $Q_{IJ}(\mathbf{x})$. In seismology, these quality factors are considered constant over the frequency band, which is usually approximated using $l = 1, \ldots, 3$ SLS mechanisms, and by solving a least-squares estimation problem to determine the y_l coefficients (Yang et al., 2016).

The spectral element discretization we use to solve these equations does not make it possible to consider fluid zones directly in the medium where the S-wave velocity would reach 0. The most common configuration we are interested in is a fluid layer on top of a viscoelastic medium. In this case, it is possible to couple partial differential equations modeling the propagation of acoustic waves in the fluid layer, with the viscoelastic equations 1 at the fluid-solid interface (the sea bottom). The acoustic equations can be modeled using the pressure P following

$$\frac{1}{\rho_f V_\mathrm{P}^2}\partial_{tt}P - \mathrm{div}\left(\frac{1}{\rho_f}\nabla P\right) = s, \tag{4}$$

where $\rho_f(\mathbf{x})$ is the fluid density, $V_\mathrm{P}(\mathbf{x})$ is the pressure velocity in the fluid, and $s(\mathbf{x},t)$ is related to a pressure source in the fluid layer. The coupling equations are

$$\begin{cases} (\partial_{tt}\mathbf{u}).\mathbf{n} = -\frac{1}{\rho_f}\nabla P.\mathbf{n}, \\ \sigma.\mathbf{n} = -P\mathbf{n}, \end{cases} \tag{5}$$

where $\mathbf{n}$ denotes the unit normal vector at the interface between the solid and the fluid layer, and σ is a three-by-three matrix corresponding to the Cauchy stress tensor. This stress tensor is related to the particle displacement vector $\mathbf{u}$ by Hooke's law, which can be written using Voigt's notations as

$$\sigma = \mathbf{CD}^T\mathbf{u}. \tag{6}$$

In the coupling equations 5, σ is remapped as a three-by-three matrix to keep homogeneity between scalars, vectors, and matrices,

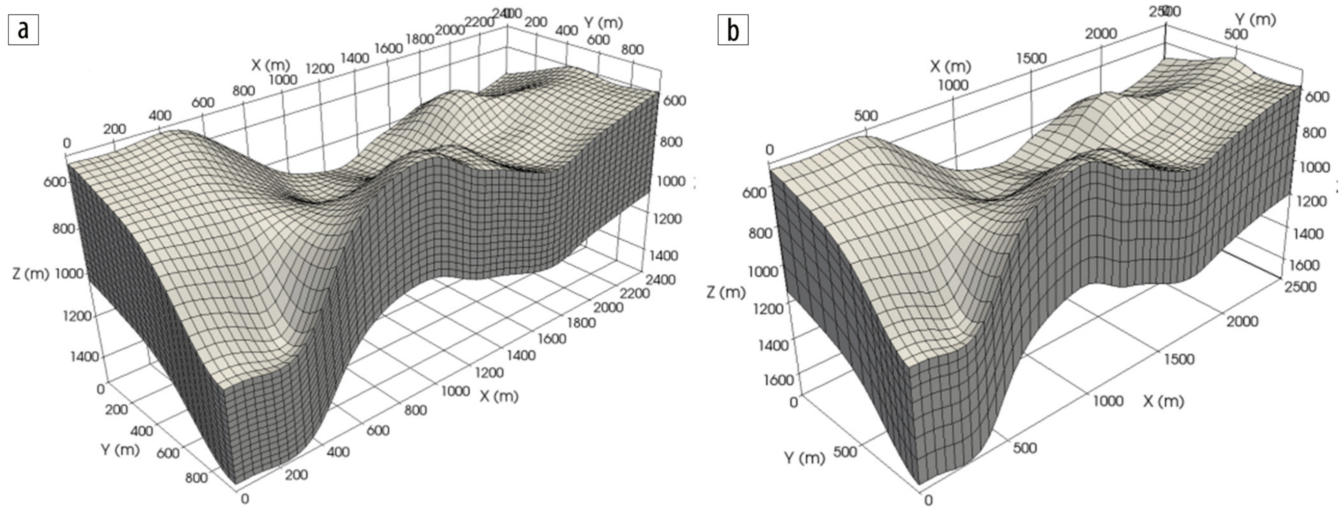

Figure 1. Two examples of a Cartesian deformed mesh with (a) constant element size and (b) variable element size.

and the quantity $\sigma.\mathbf{n}$ is to be understood as the reduction from a three-by-three matrix to a three-component vector.

The first coupling condition implies the continuity of the normal component of the acceleration at the interface. The second equation implies the continuity of the normal stress at the interface.

To accurately model interface waves, we need to accurately accommodate for the solid-air interface (land configuration) or the solid-water interface (marine configuration). This is possible using conventional finite-difference schemes on Cartesian grids, but it remains difficult, with such discretization methods, to control the balance between accuracy and computational cost in case of highly varying topography/bathymetry (de la Puente et al., 2014).

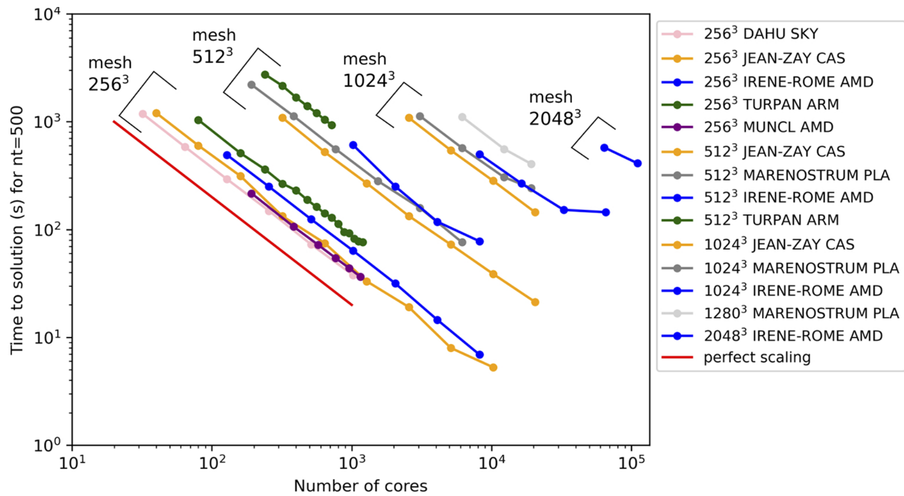

Figure 2. Parallel efficiency assessed for a forward fully elastic modeling engine on different HPC CPU-based machines with different architectures: Intel (SKYlake, CAScade lake, PLAtinum), AMD Rome Epyc (IRENE-ROME), AMD Genoa 9654 (MUNCL), and ARM Ampere Altra (TURPAN).

We prefer using a continuous finite-element discretization method, namely the spectral element method. This approach relies on Lagrange polynomials defined on a hexahedral mesh, and Gauss-Lobatto-Legendre (GLL) discretization points to evaluate the integrals. This choice guarantees the continuity of the solution across the mesh elements without any additional constraints because the GLL points contain the points at the element boundaries. In addition, through the weak-form solution, the free surface condition or the coupling conditions in the fluid-solid case are satisfied.

The specificity of our implementation relies on the following points. To simplify the implementation and speed up the overall efficiency, we rely on a Cartesian-based mesh only vertically deformed to conform to the free surface/bathymetry interfaces (Figure 1). This avoids the use of lookup tables when we loop over the elements. Our implementation relies on fourth- and fifth-order Lagrange polynomials, which in practice provides a good trade-off between accuracy and computational efficiency. We authorize the use of arbitrary order polynomial for the shape functions describing the free surface or bathymetry interfaces. For the time discretization, a second-order predictor-corrector Newmark scheme is used.

Our implementation results in the SEM46 software, which has more than 100,000 lines of code. It is written in Fortran 90, and the high-performance computing (HPC) implementation is based on a two-level message passing interface parallelization: the inner level performs a domain decomposition over the Cartesian-based structured mesh; the outer level manages multiple sources in parallel to handle computation with a large number of virtual/active shots in FWI applications. SEM46 has been tested on various HPC architectures and shows almost perfect linear scalability (Figure 2). The largest problem considered so far represents a 2048^3 fourth-order elements mesh using up to 110,582 CPU cores.

Note that for the two case studies presented in this paper, FWI is performed in the elastic or acoustic-elastic approximation, without taking into account the attenuation. The motivation is to save computational time, while we expect the sensitivity to attenuation to be reduced, as in both cases we consider relatively low- and narrow-frequency bands, and we use a misfit function focused on the phase and not the amplitude. Still, SEM46 offers the possibility to account for attenuation on P and S waves, both in the modeling step or in the inversion step.

Interferometry of ambient seismic noise. The emergence of the Green's function between two stations from the averaging of the correlation of the signal they record represents a breakthrough in seismology (Campillo, 2006). Compared with exploration seismic, earthquake-based seismology is severely constrained by the uncontrolled nature of the sources. Earthquakes occur mostly along faults, resulting in a sparse illumination of the subsurface. Their occurrence is unpredictable, and their precise location, mechanism, and temporal signature is unknown. The ability to recover the interstation Green's functions from passive data recorded by a network of stations is thus valuable help.

The first theoretical result came from acoustic and statistical physics: when the wavefield enters in a diffusion regime, either generated by multiple scattering or the stimulation from random sources (or a combination of both), a discrete modal decomposition of the wavefield shows that the cross-correlation of the signal recorded by two stations, averaged over different realizations, converges toward the interstation Green's function (Lobkis and Weaver, 2001).

Approximately at the same time, studies on time-reversal techniques for a single acoustic source in a reverberant cavity reached the same result. Extension to opened media and to waveguides configurations were shown to be possible provided a suitable distribution of acoustic sources is used (e.g., Derode et al., 2003).

The extension of these results to elastic waves at regional scale for seismology was not straightforward, at least from a theoretical point of view. The question asked at that time was whether it is possible to record an elastic wavefield propagating in the earth in a diffusive state, characterized by an equipartition of the energy between P and S modes, before it is attenuated. Inspired by the work on coda waves initiated by Aki (1957), Campillo and Paul (2003) showed experimentally that cross-correlations of coda waves converge toward the Green's function between a pair of stations.

This result had been conjectured in the exploration seismic community decades before. In an early work, Claerbout (1968) showed how the autocorrelation of the recording of transmitted data from a surface receiver in a layered earth converges toward the impulse response at the receiver location. This impulse response can then be used to image the reflectivity below the receiver. In the conclusion of his paper, Claerbout conjectured that the Green's function between two receivers could be extracted from the cross-correlation of the recorded transmitted signal. This field of research remained active in the exploration community under the name of acoustic daylight imaging (Rickett and Claerbout, 1999; Schuster et al., 2004). This technique is actually interferometry applied to seismic imaging: cross-correlograms of passive data are inverted to build reflectivity images or to localize sources.

Wapenaar (2003) first demonstrated the conjecture of Claerbout in 3D acoustic for layered media, and then extended this result to 3D general elastic media, with surface passive recordings (Wapenaar, 2004). What is perhaps the most striking is that the demonstration in Wapenaar (2004) does not make any statistical assumption: the obtained result follows a purely deterministic approach. Yet, this equivalence result relies on strong assumptions. For the cross-correlation of the recorded signals to be equal to the elastic Green's function, the pair of stations should record separately the elastic wavefields generated by volume forces and deformation rate sources deployed continuously along an arbitrary surface below the two stations. However, introducing the assumption of mutually uncorrelated random noise sources at depth, a result similar to Lobkis and Weaver (2001) was obtained, formalizing the theoretical extension of this result to the elastic approximation.

Because the distribution and the energy of noise sources cannot be easily taken into account in practice, the absolute amplitude reconstruction is not guaranteed. However, the actual waveform shape is recovered, which makes it possible to invert for the phase information in the frame of elastic FWI. The motivation is to increase the resolution of the subsurface images derived from this passive data compared with conventional tomography techniques. The problem is formulated as follows. For two stations at x_A and x_B, the observed data can be written as

$$d_{obs}(x_A, x_B) = G(x_A, x_B, t) * w(t), \tag{7}$$

where $G(x_A, x_B)$ is the Green's function from x_B recorded in x_A, $*$ denotes the convolution operation, and $w(t)$ is a wavelet acting as a band-pass filter. The inverse problem we solve is

$$\min_m \sum_{x_A} \sum_{x_B} F\left(d_{cal}[m](x_A, x_B), d_{obs}(x_A, x_B)\right), \tag{8}$$

where F denotes a multitaper misfit function, as proposed in Tape et al. (2010). This misfit function measures the sum of the squares of the frequency-dependent phase-traveltimes differences. Moreover, m denotes the subsurface parameters we invert for, derived from the density ρ and the stiffness tensor C (i.e., P- and S-wave velocities), and $d_{cal}[m](x_A, x_B)$ is computed as

$$d_{cal}[m](x_A, x_B) = u_{x_B}[m](x_A, t) * w(t), \tag{9}$$

with $u_{x_B}(\mathbf{x}, t)$ solution of the coupled acoustic/viscoelastic equations 1, 4, and 5 for a source term located in x_B.

Harmalière landslide case study

The Harmalière (HAR) landslide, in the French western Alps, is a slow-moving landslide affecting a 2 km^2 area (Figure 3a). It is characterized by a landslide-prone fine-grained Quaternary unit with a thickness ranging between 0 and 250 m. This unit consists of alternating glacio-lacustrine laminated silt and clay and nonlaminated lacustrine sediments mixed with moraines (Figure 3b). HAR shows sudden reactivations (March 1981 and June 2016 recently, Lacroix et al., 2018), suggesting the role of local subsurface heterogeneities. In addition, the central part of HAR varies between a plastic slide at the top and a fluid flow at the toe (Figure 3b).

Within the RESOLVE project (Gimbert et al., 2021), in May-June 2021, a dense 3D array of broadband geophone nodes has been deployed to record continuously natural seismicity for a one-month period in the HAR site, as well as 3D active-source data set (Figure 3).

We use the ambient noise recordings to extract interstation Green's function by cross-correlating independent pair of stations. Data are preprocessed using the following workflow. A low-pass filter to limit the frequency content below 3.5 Hz is applied. The time series are normalized by the value of the envelope, thus equalizing the contributions of weak and strong signal and attenuating the impact of short high-amplitude transients (e.g., microearthquake, slide-quakes). Each 24-hour time window is divided into 15-minute-long subtime windows, on which normalized cross-correlation (cross-coherence) is calculated in a range of time lags between (-7.,7.) s. Cross-coherence is performed in the frequency domain, where a power-spectrum normalization is added with respect to conventional cross-correlation, thus effectively implementing for each data chunk a spectral whitening. Finally, the 14 s long (-7,7) cross-coherence functions are phase-weighted stacked, and a virtual-source gather is obtained for each station (Figure 4).

Elastic FWI is applied on the resulting interstation Green's functions. The starting V_S model is built using ambient noise tomography from the same Green's functions. The starting V_P model is built by tomography from active data acquired with hammer sources at the deployment time. The topography to model wave propagation here is crucial. It is extracted and resampled from a 1 m resolution LiDAR airborne survey (Provenzano et al., 2024).

The final V_S model shows significant broadband updates with respect to the starting ambient noise tomography model, both in shallow and deep subsurface, with higher values at depths between 40 and 70 m, as well as a sharper low-velocity anomaly in the southmost part of the model (Figure 5). In this 1.3–3.0 Hz band, elastic FWI converges after nine iterations, reducing the misfit value to about 45% of the initial one. This corresponds to an increased waveform alignment for most traces at the measurement windows, although the relatively high misfit plateau reflects the nonreproducibility of the full cross-correlation waveforms at some locations (Figure 6).

Previous geologic studies highlighted a modification of the landslide's deformation mechanism from a slide (plastic-like) at the top (x < 400 m) to a flow (fluid-like) at the toe (x > 400 m), with open questions regarding the mechanisms controlling the transition zone between these two regimes (Fiolleau et al., 2021). The S-wave velocity model reconstructed here brings a first answer. At about x = 425 m, an increase in the S-wave velocity model from 200 m depth to a few tens of meters below the surface is visible, drawing a bulge-like structure. It is already present in the ambient noise tomography model and reinforced in the FWI model. This could correspond to consolidated, relatively rigid clay. Farther away from this point, toward the south, the S-wave velocity significantly decreases, which could correspond to the less consolidated, flowing part of the landslide. The reason for the transition between the two regimes could be this vertical heterogeneity. The material sliding from the headscarp moves southward and accumulates in this central zone, probably because it is blocked by the rigid bulge. Once the increase in shear stress caused by increasing accumulation reaches a critical threshold (Carrière et al., 2018), the material flows southward.

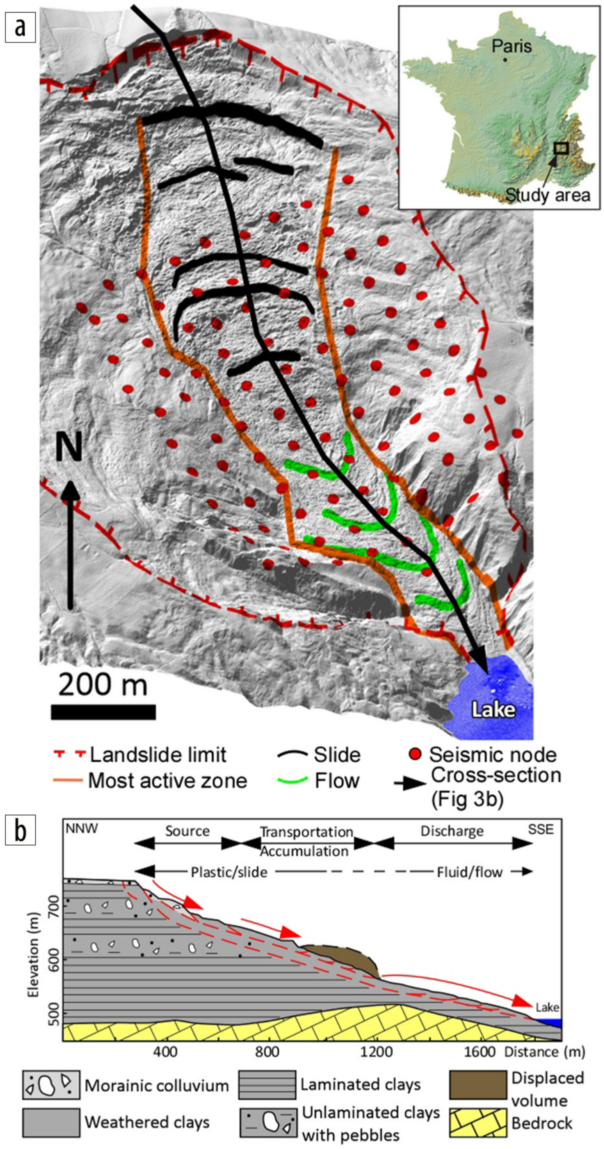

Figure 3. (a) Localization of the HAR landslide and overview of the acquisition deployment. The red dots represent the geophone array positions. (b) Geologic cross section along the central, active part of the HAR landslide, representing the current state of knowledge of the survey area.

Western Alps and Ligurian Sea case study

The results we present here are extracted from Nouibat et al. (2023). In the complex tectonic setting of the Alps and northwestern Mediterranean, a precise seismic mapping of the 3D structure of Moho is crucial to understand the deep dynamic processes involved in the orogenesis of the western Alps and the opening of the Ligurian-Provence back-arc basin. With the deployment of the AlpArray temporary seismic network, Western Europe has become one of the most densely instrumented areas in the world. We have computed vertical component cross-correlations between 600 broadband stations from all available temporary and permanent networks in the Alpine region (Figure 7, 2°E-16.2°E; 41.3°N-49.1°N) during the 2015–2019 period. The station array includes the entire AlpArray Seismic Network (AASN) and the Cifalps-2 experiment. The offshore component of the data set consists of high-quality correlations between the AASN OBSs (Nouibat et al., 2022b).

We keep only reliable cross-correlations by applying the following criteria: (1) signal-to-noise ratio greater than 5, (2) difference in group velocity measured on the positive and negative parts less than 0.2 km/s, and (3) interstation distance larger than one wavelength for the maximum period considered in each period band. The final data set includes approximately 22×10^3 to 55×10^3 high-quality cross-correlations depending on the period band. For FWI, all stations in Figure 7 serve as receivers, out of which 185 stations are used as virtual sources (white circles).

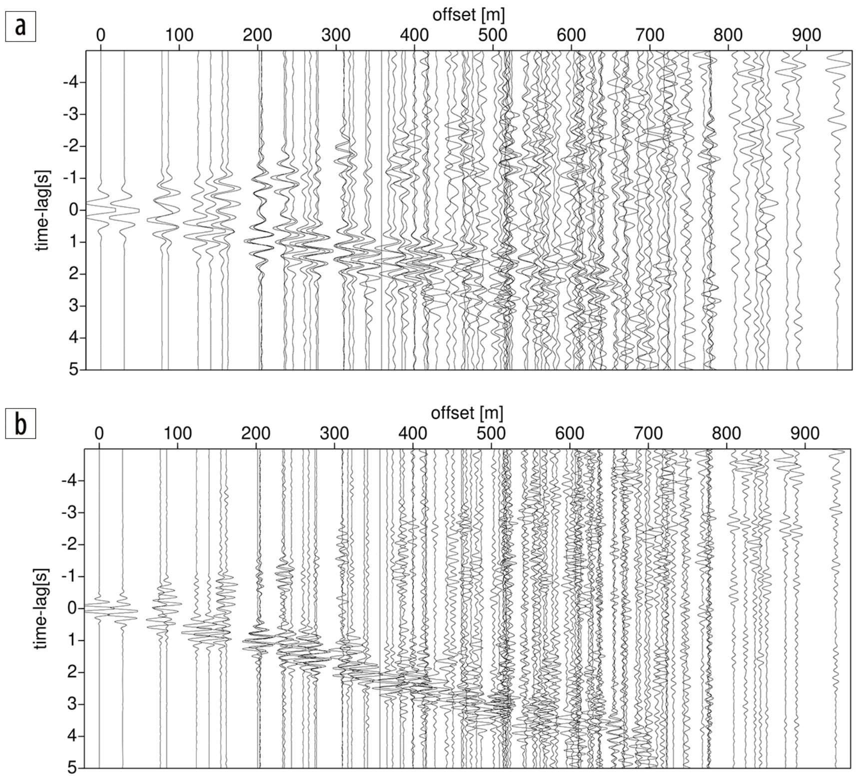

Figure 4. Example cross-coherence noise function for negative and positive time lags, sorted in increasing offset with respect to the reference station. Dispersive surface waves emerge from the ambient noise interferometry with higher wavespeeds at lower frequencies: (a) 1.5–2.5 Hz, (b) 3.0–5.0 Hz.

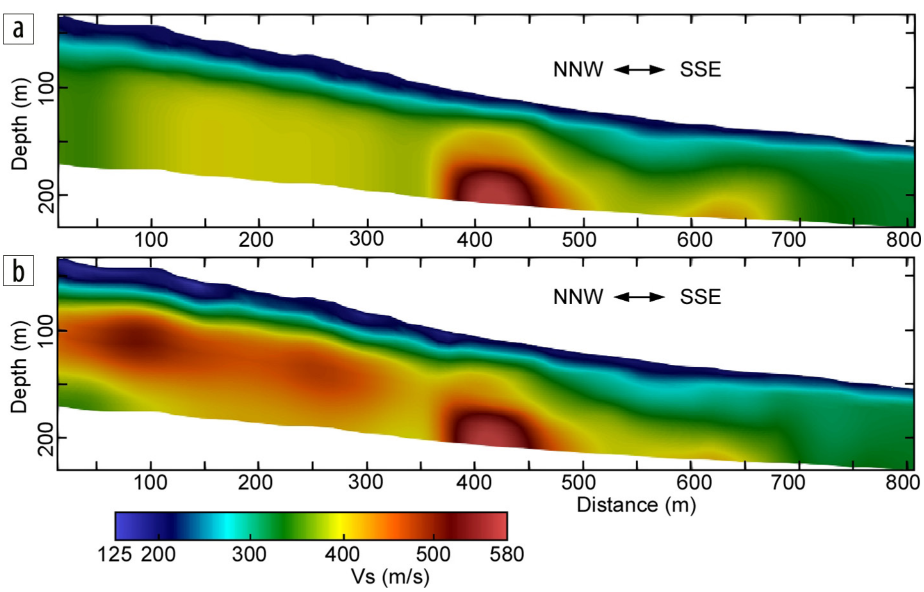

Figure 5. Vertical north–south slice cutting through the middle of the volume. (a) Ambient noise tomography (starting) model. (b) Final elastic FWI model. Note that the updates remain relatively shallow (z < 150 m depth). The reason is the reconstructed interstation Green's function from noise data contain mostly surface waves, which decay exponentially fast away from the solid/air interface, and thus have a limited depth penetration, around 0.4 times the dominant wavelength.

The initial model consists of the pseudo-3D onshore-offshore V_S model obtained from Bayesian ambient noise tomography by Nouibat et al. (2022a, 2022b), and a V_P model converted from this V_S by the Brocher formula: $V_P = 0.9409 + 2.0947V_S - 0.8206V_S^2 + 0.2683V_S^3 - 0.0251V_S^4$. We reconstruct simultaneously V_S and V_P to account for the sensitivity of the Rayleigh wave to V_P, which becomes nonnegligible at short periods. We employ a randomized subsampling strategy of the ensemble of virtual sources over iterations to reduce the computational cost.

Figure 8 shows the depth slices of the initial and final V_S models at 6 km (Figures 8a1 and 8a2) and 26 km (Figures 8b1 and 8b2) and corresponding relative variations (Figures 8a3 and 8b3). We observe strong relative variations. At 6 km depth, the final model exhibits lower velocities (≤ 2.5 km/s) with strong negative velocity variations (≤ −8%) in the Ligurian-Provence Basin. These low velocities probably reflect the slow propagation of Rayleigh-Scholte waves, induced by the sedimentary cover. Another pattern appears in Corsica where the western Variscan Corsica (see Figure 7) exhibits higher velocities (≥ 3.5 km/s) than the northeastern Alpine Corsica. Such variations are probably due to Rayleigh-Scholte mode conversions across the Corsican Margin, which are taken into account by the 3D fluid-solid coupling. On the onshore domain, relative variations roughly coincide with geologic structures, with a velocity decrease in the western and eastern parts of the subduction wedge and an increase in the forelands.

Based on these results, a new 3D Moho map of the western Alps region (Figure 9c) is derived, estimated from the depth of the iso-velocity surface V_S = 4.2 km/s. In the southwestern Alps, while Lu et al.'s (2020) model exhibits

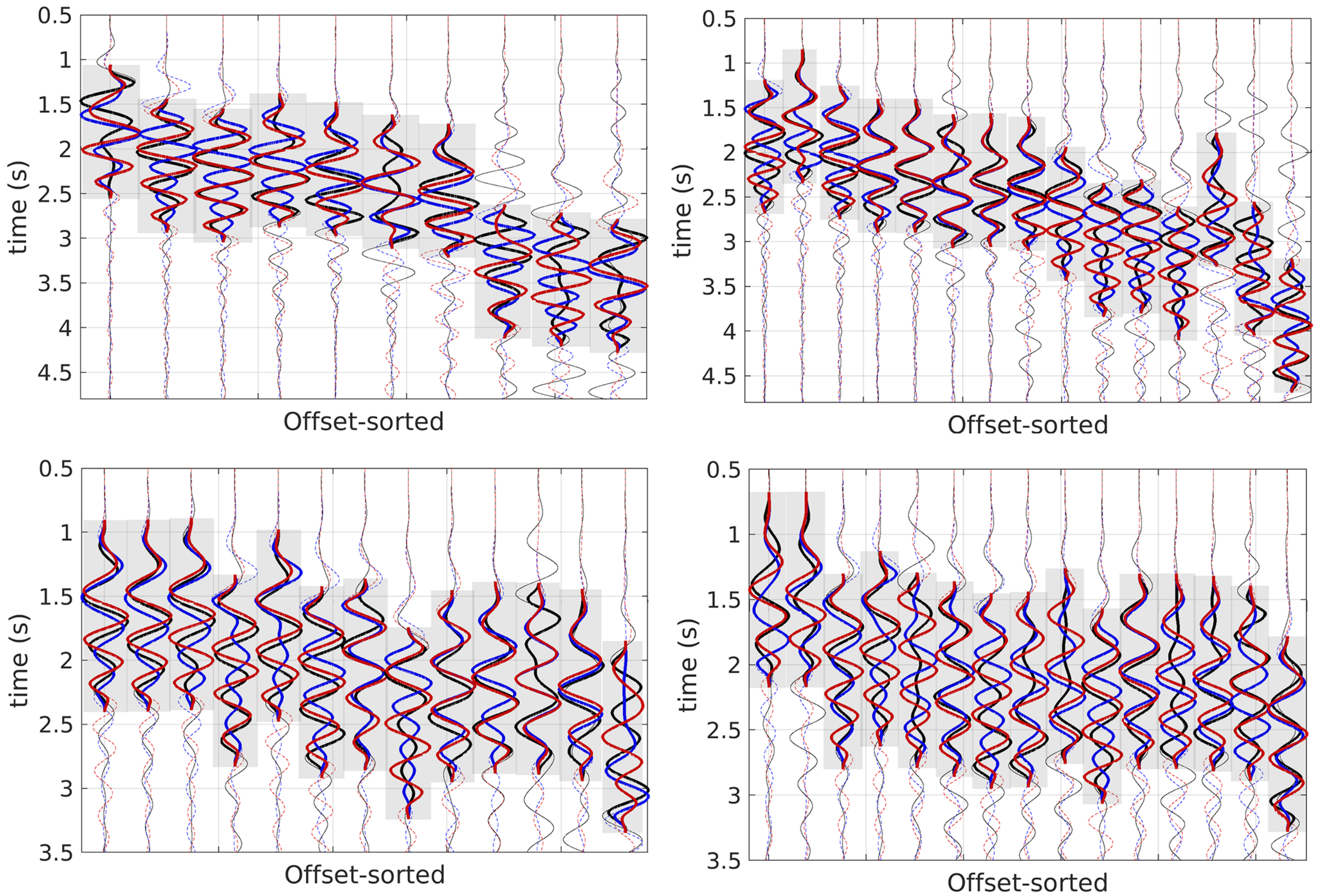

Figure 6. Trace-by-trace waveform data fit. Black: observed data. Blue: computed data in the starting model. Red: computed data in the final model. Traces are sorted in ascending absolute offset, but offset interval is irregular reflecting the three-dimensional acquisition.

approximately 40–45 km depths, the Moho in our model deepens to depth greater than 60 km, which is more consistent with the continental subduction from receiver functions (RF) observations (Zhao et al., 2015). We also obtain a shallower Moho (20–25 km) associated with the Ivrea Body (white dashed line on Figure 9c). The strong along-strike variations in our Moho depth from north to south are in line with RF observations between the northwestern and southern Alps (Paul et al., 2022), indicating a noncylindricity of the deep structure of the western Alps.

Figure 10 shows snapshots of the simulated vertical displacement recorded at the surface, in the 5–10 s period band for an onshore source station located in southern France. We compare elastic (Figures 10a1–10c1) and acoustic-elastic modeling (Figures 10a2–10c2) in the initial model to emphasize the importance of taking into account the fluid

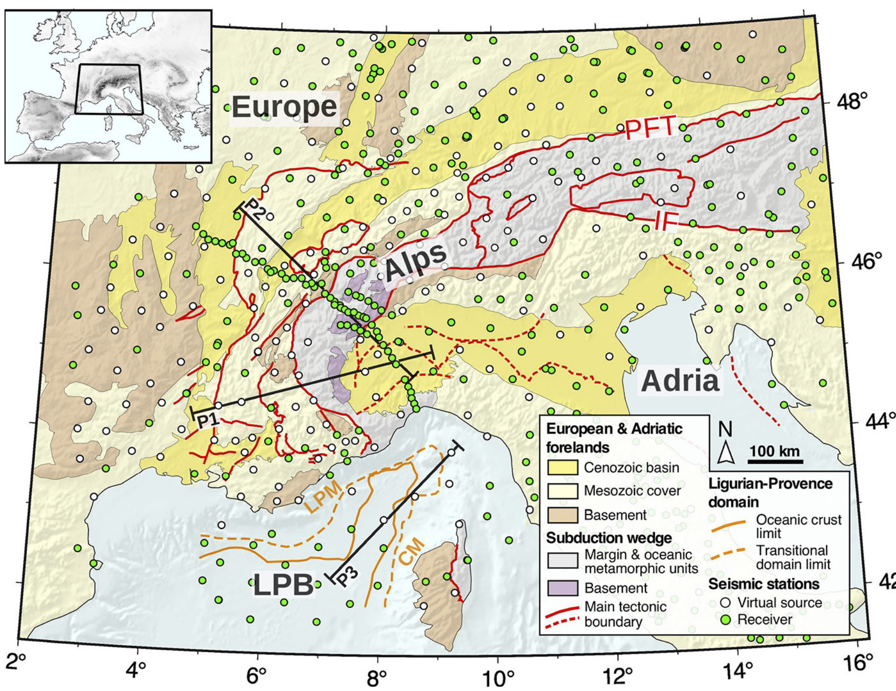

Figure 7. Geologic and tectonic setting of the study area, with locations of seismic stations used in this work (white circles: virtual sources; green circles: receivers). LPB: Ligurian-Provence Basin, LPM: Ligurian-Provence Margin, CM: Corsican Margin. Figure extracted from Nouibat et al. (2023).

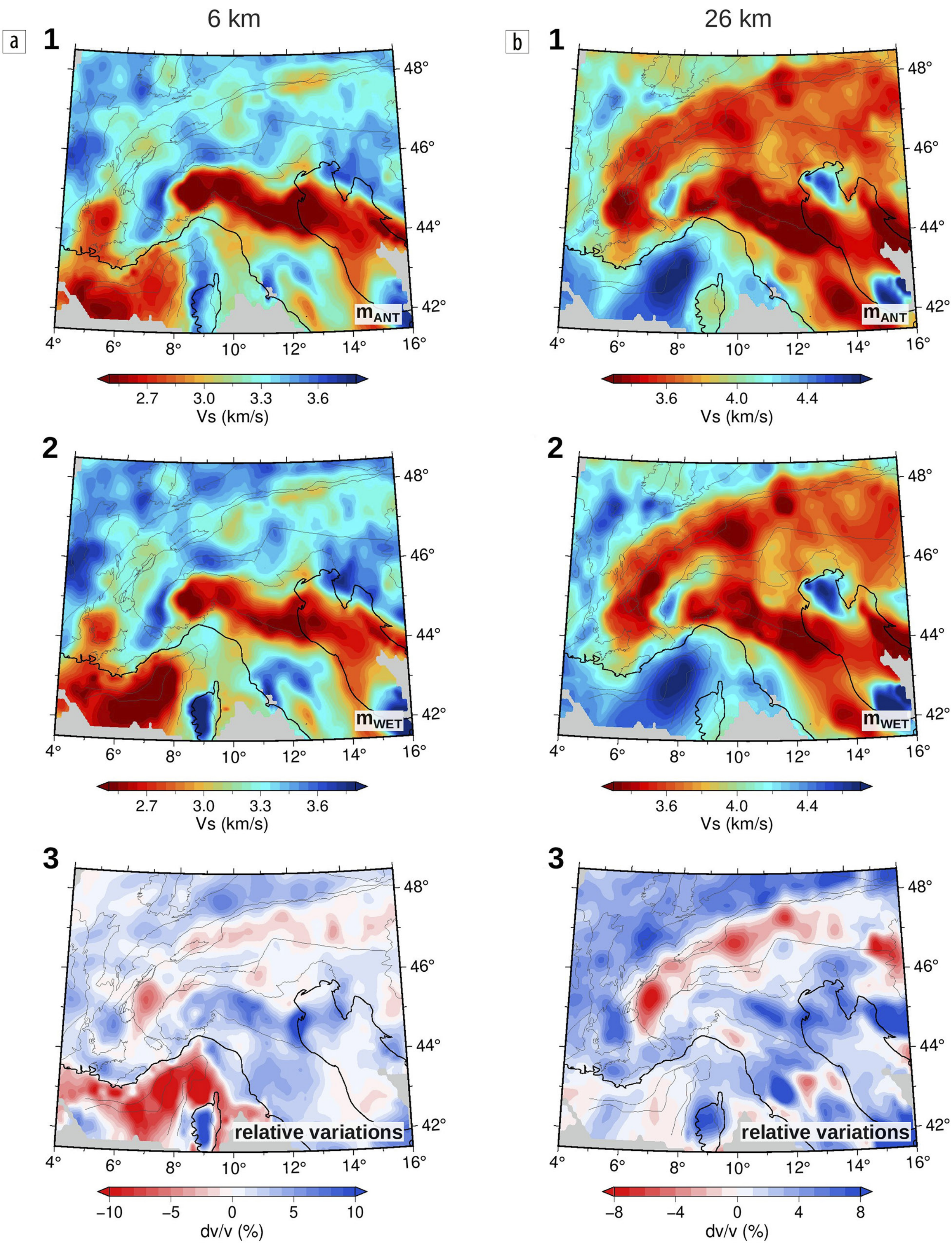

Figure 8. Depth slices in (a1, b1) the initial and (a2, b2) final shear-wave velocity models and the relative variations to the initial model (a3, b3), at 6 km (a1–a3) and 26 km (b1–b3) depths. Figures extracted from Nouibat et al. (2023).

layer. Figure 11 shows synthetic waveform fits to data at an OBS located in the central Ligurian-Provence Basin at a depth of approximately 2700 m (location in Figure 11a). Figures 11b1, 11b2, 11c1, 11c2, 11d1, and 11d2 show simulations in the initial model and Figures 11b3, 11c3, and 11d3 show simulations in the final model. In the elastic modeling case, the source–OBS pair is assumed to be located on the free surface, which is why we observe the propagation of a Rayleigh wave in the oceanic part (Figures 10a1–10c1). In the acoustic-elastic case, we observe a mode conversion from Rayleigh to Rayleigh-Scholte wave at the Gulf of Lion Margin (Figures 10a2–10c2). The resulting wave packet is characterized by stronger amplitude and slower propagation velocity and includes strong wavefront distortions. However, we notice in both cases a dissipation within the Ligurian-Provence Basin and

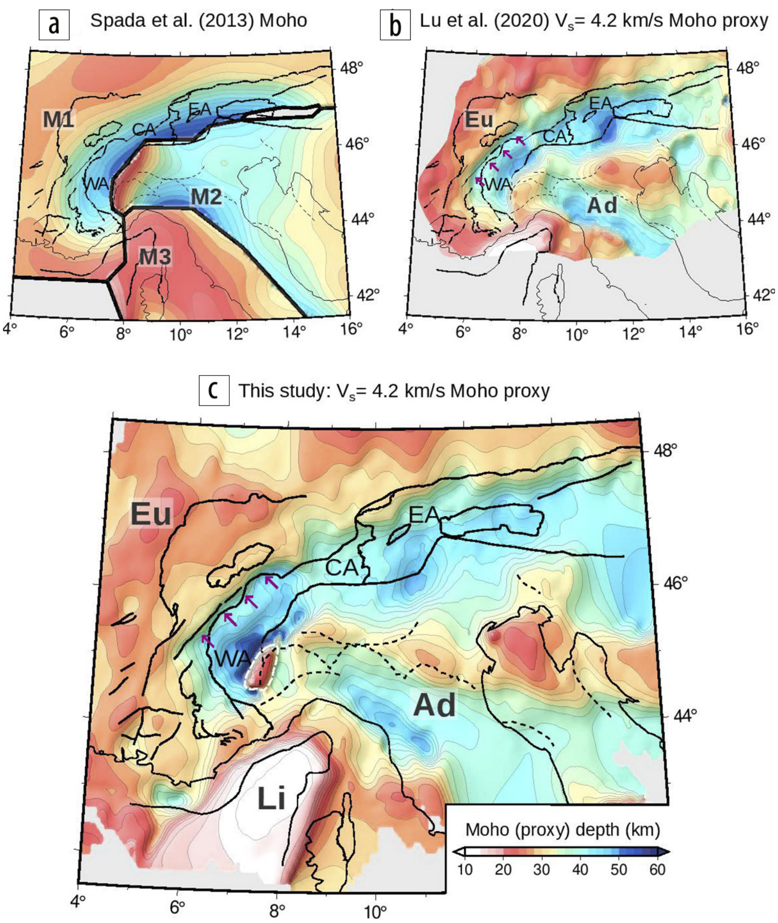

Figure 9. Depth maps of Moho and Moho proxy in the Alps and Northwestern Mediterranean. (a) Spada et al.'s (2013) map composed of three blocks: European Moho (M1), Adriatic Moho (M2) and Ligurian–Sardinia–Corsica–Tyrrhenian Moho (M3). (b) Lu et al. (2020)'s depth map of the V_S = 4.2 km/s iso-velocity surface from their WET model. (c) Depth map of the V_S = 4.2 km/s iso-velocity surface from our WET model. For a better illustration, the color scale is saturated at 60 km depth. Acronyms: Eu: European Moho; Ad: Adriatic Moho; Li: Ligurian Moho; WA: western Alps; CA: central Alps; EA: eastern Alps. Arrows in purple: Moho step beneath the external crystalline massifs. Dashed white line: shallow Moho associated with the Ivrea Body. The gray areas hide regions where Moho maps are unconstrained. Figures extracted from Nouibat et al. (2023).

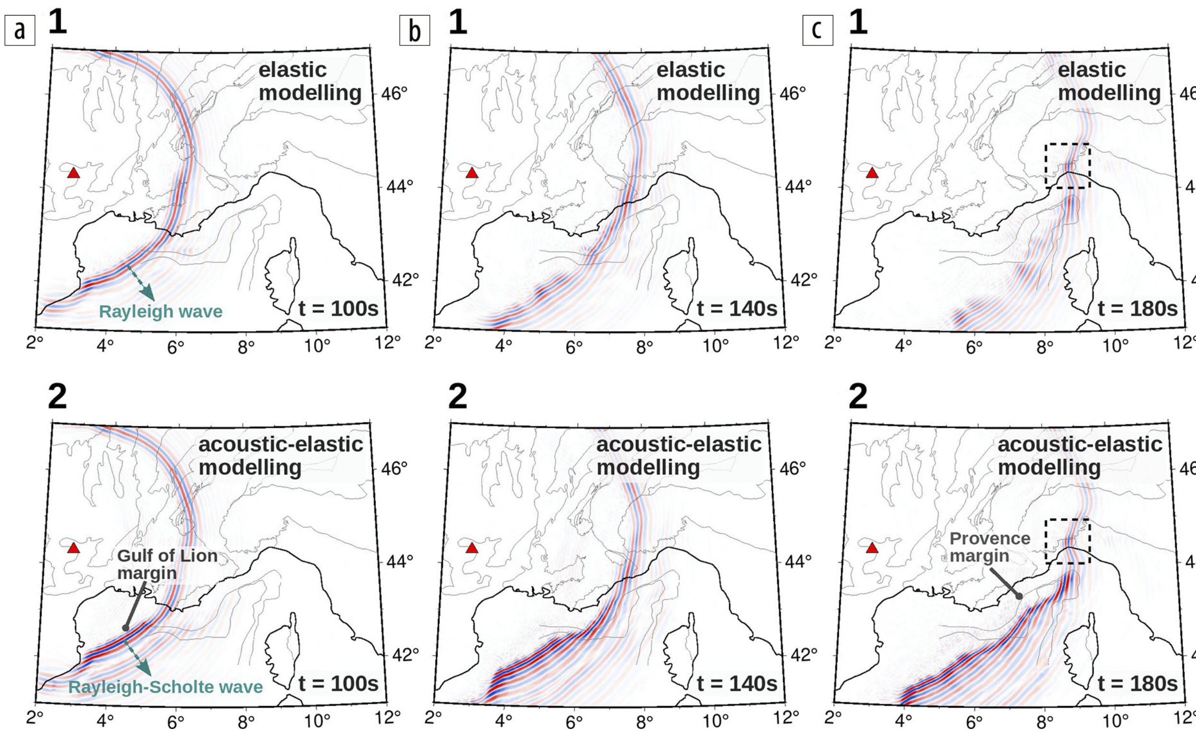

Figure 10. Comparison of snapshots of the vertical displacement wavefield in the 5–10 s period band, simulated using (a1–c1) the elastic wave equation, (a2–c2) the acoustic-elastic coupled wave equation, for the source station indicated by the red triangle. The wavefields are extracted on a 3D surface corresponding to the topography in the onshore part and to the bathymetry of the seafloor in the marine part. Black dashed frames show scattered Rayleigh-wave packets. The thin black lines are geologic and tectonic boundaries from Figure 7. Figures extracted from Nouibat et al. (2023).

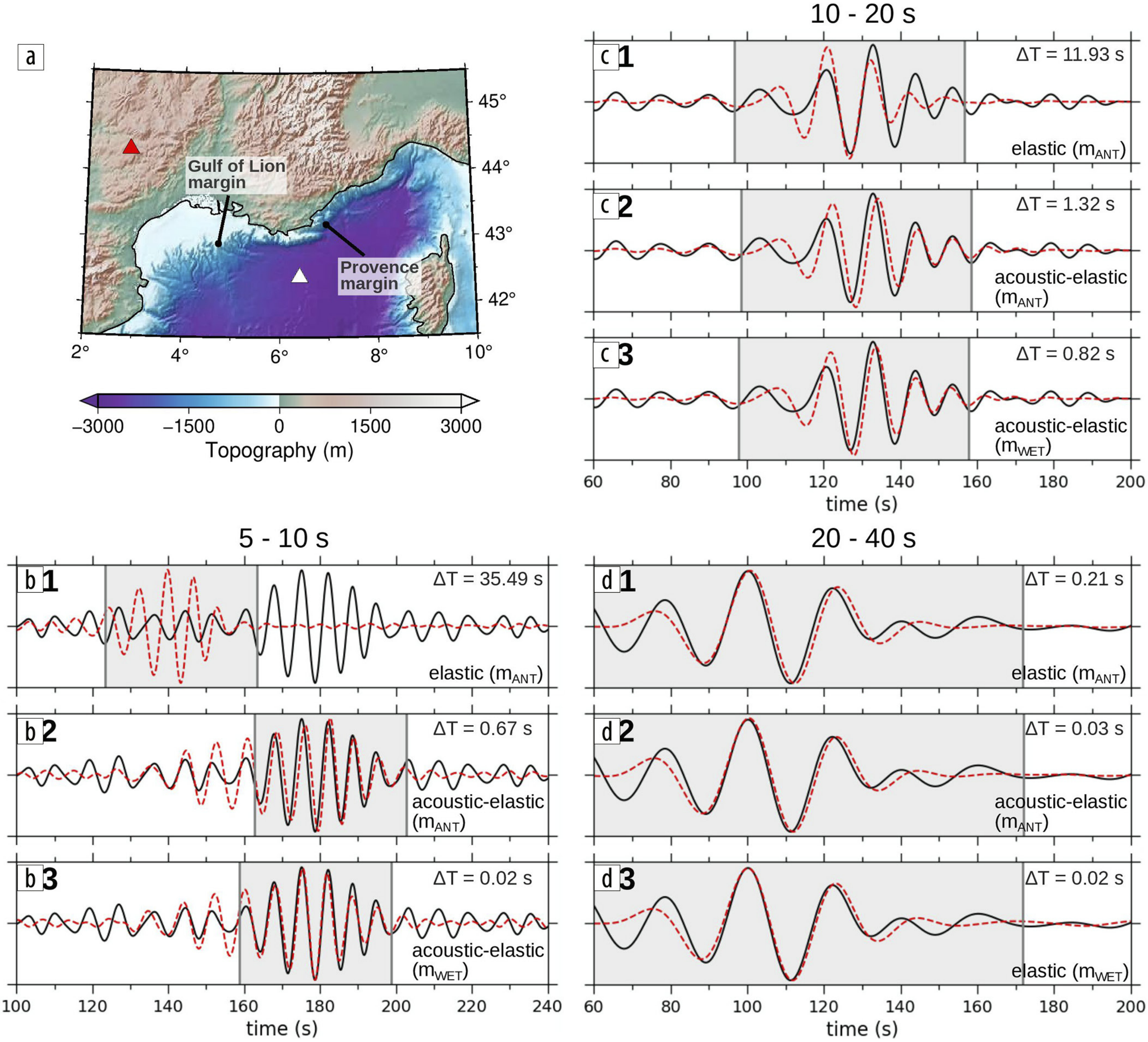

Figure 11. Comparisons between simulated vertical-component seismograms (red) and observed noise correlation waveforms (black), filtered in the 5–10, 10–20, and 20–40 s period bands, for the source-receiver pair in (a) (red: station source, white: receiver). Elastic and acoustic-elastic simulations in the initial model (m_{ANT}) are shown in b1, c1, d1 and b2, c2, d2 respectively. Seismograms in b3, c3 are computed from acoustic-elastic modeling in the final model (m_{WET}) while d3 is computed from elastic modeling. The gray areas indicate the surface-wave window and ΔT corresponds to the cross-correlation-based time shift between observed and synthetic windowed waveforms. Figures extracted from Nouibat et al. (2023).

almost the same wavefield in the continental part. For instance, both simulations evidence a scattering of the wave packet to the north of the Ligurian Sea (dashed black frame in Figures 2c1 and 2c2).

The discrepancies in amplitude and traveltime in the oceanic part are significant. The arrival time of the Rayleigh-wave envelope obtained from elastic modeling in the 5–10 s band is approximately 35 s earlier than that of the Rayleigh-Scholte wave obtained from acoustic-elastic modeling (Figures 11b1 and 11b2). Furthermore, the arrival time of the observed surface wave is much closer to the arrival time of the simulated signal with fluid-solid coupling (Figure 11b2). This fit is further improved after inversion as shown in Figure 11b3. Differences between the two modeling results are also visible in the 10–20 s period band with a lower but still significant misfit due to the free surface boundary condition (Figures 11c1–11c3).

Conclusion and perspectives

Elastic FWI is appealing, as it is able to better account for the wave propagation within the subsurface and to provide simultaneous reconstruction of P- and S-wave velocities. This in turn refines our characterization of the subsurface. Recent applications in the Gulf of Mexico have shown already the interest in applying elastic FWI to improve the AVO response and better delineate salt bodies in the P-wave velocity reconstruction (Rivera et al., 2019).

However, elastic FWI remains challenging because of its high computing cost, the need for appropriate numerical tools, and the increased nonlinearity of the FWI problem itself. Regarding this point, we believe that taking benefit of the more and more frequent deployment of OBS, to retrieve interstation Green's functions by interferometry strategies and invert them through FWI is an interesting opportunity.

In this study, we have shown two examples of such strategy, at different scales — one for the characterization of a landslide in a near-surface imaging configuration, the other for imaging the western Alps and Ligurian Sea. In both cases, the reconstructed velocity models provide useful information to characterize the subsurface.

The computational cost associated with elastic FWI in high-frequency bands still appears as a limiting factor. To overcome this limitation, the capability of running on different hardware, including GPU (Cao et al., 2022), is fundamental. Within the SEISCOPE project, we are currently designing an FWI orchestrator that distributes the computational request on potentially heterogeneous hardware in an asynchronous way, to more efficiently exploit HPC infrastructures, in the perspective of exascale computing (Schuster et al., 2024).

The strong nonlinearity of elastic FWI also calls for the design of robust inversion strategies. In this frame, a better exploitation of the multicomponent data accessible through OBS is also an interesting lead to follow. In recent work, we have shown how a time-dependent polarization attribute can be extracted from multicomponent data and used to design a polarization-based misfit function that is more robust and less sensitive to prior knowledge of the source time-signature (Sambolian et al., 2022).

Finally, elastic FWI is not only a computer-intensive and highly nonlinear problem, it is also a multiparameter inverse problem, for which dedicated inversion strategies are needed to mitigate parameter coupling (Operto et al., 2013). Truncated Newton strategies could be deployed using recent techniques (Yong et al., 2022). We also believe that regularization strategies based on homogenization should be considered (Capdeville and Métivier, 2018). The latter theory shows that subwavelength subsurface heterogeneities are "sensed" by the wavefield as a local anisotropy, which in turn suggests that an FWI reconstructed model is at best a homogenized version of the true model. This provides a way to reduce the effective null space by projecting the FWI updates on the space of equivalent homogenized media. This is a work that we will pursue in the future. TLE

Data and materials availability

Data associated with this research are available and can be obtained by contacting the corresponding author.

Corresponding author: ludovic.metivier@univ-grenoble-alpes.fr

References

Aki, K., 1957, Space and time spectra of stationary stochastic waves, with special reference to microtremors: Bulletin of the Earthquake Research Institute, **35**, 415–456.

Campillo, M., 2006, Phase and correlation in 'random' seismic fields and the reconstruction of the green function: Pure and Applied Geophysics, **163**, no. 2–3, 475–502, https://doi.org/10.1007/s00024-005-0032-8.

Campillo, M., and A. Paul, 2003, Long-range correlations in the diffuse seismic coda: Science, **299**, no. 5606, 547–549, https://doi.org/10.1126/science.1078551.

Cao, J., R. Brossier, E. Cabrera, J. de la Puente, L. Métivier, and A. Tarayoun, 2022, GPU accelerated computing towards a fast and scalable seismic wave modelling in SEISCOPE SEM46 code: Presented at the Sixth EAGE Workshop on High Performance Computing, EAGE.

Capdeville, Y., and L. Métivier, 2018, Elastic full waveform inversion based on the homogenization method: Theoretical framework and 2-D numerical illustrations: Geophysical Journal International, **213**, no. 2, 1093–1112, https://doi.org/10.1093/gji/ggy039.

Carcione, J., D. Kosloff, and R. Kosloff, 1988, Wave-propagation simulation in an elastic anisotropic (transversely isotropic) solid: The Quarterly Journal of Mechanics and Applied Mathematics, **41**, no. 3, 319–346, https://doi.org/10.1093/qjmam/41.3.319.

Carrière, S., D. Jongmans, G. Chambon, G. Bièvre, B. Lanson, L. Bertello, M. Berti, M. Jaboyedoff, J.-P. Malet, and J. Chambers, 2018, Rheological properties of clayey soils originating from flow-like landslides: Landslides, **15**, no. 8, 1615–1630, https://doi.org/10.1007/s10346-018-0972-6.

Claerbout, J. F., 1968, Synthesis of a layered medium from its acoustic transmission response: Geophysics, **33**, no. 2, 264–269, https://doi.org/10.1190/1.1439927.

de la Puente, J., M. Ferrer, M. Hanzich, J. E. Castillo, and J. M. Cela, 2014, Mimetic seismic wave modeling including topography on deformed staggered grids: Geophysics, **79**, no. 3, T125–T141, https://doi.org/10.1190/geo2013-0371.1.

Derode, A., E. Larose, M. Tanter, J. De Rosny, A. Tourin, M. Campillo, and M. Fink, 2003, Recovering the Green's function from field-field correlations in an open scattering medium (L): The Journal of the Acoustical Society of America, **113**, no. 6, 2973–2976, https://doi.org/10.1121/1.1570436.

Fiolleau, S., D. Jongmans, G. Bièvre, G. Chambon, P. Lacroix, A. Helmstetter, M. Wathelet, and M. Demierre, 2021, Multi-method investigation of mass transfer mechanisms in a retrogressive clayey landslide (Harmalière, French Alps): Landslides, **18**, no. 6, 1981–2000, https://doi.org/10.1007/s10346-021-01639-z.

Gimbert, F., U. Nanni, P. Roux, A. Helmstetter, S. Garambois, A. Lecointre, A. Walpersdorf, et al., 2021, A multi-physics experiment with a temporary dense seismic array on the Argentière glacier, French Alps: The RESOLVE project: Seismological Research Letters, **92**, no. 2A, 1185–1201, https://doi.org/10.1785/0220200280.

Lacroix, P., G. Bièvre, E. Pathier, U. Kniess, and D. Jongmans, 2018, Use of Sentinel-2 images for the detection of precursory motions before landslide failures: Remote Sensing of Environment, **215**, 507–516, https://doi.org/10.1016/j.rse.2018.03.042.

Lailly, P., 1983, The seismic inverse problem as a sequence of before stack migrations: Presented at the Conference on Inverse Scattering, Theory and Application, Society for Industrial and Applied Mathematics, 206–220.

Lobkis, O., and R. Weaver, 2001, On the emergence of the Green's function in the correlations of a diffuse field: The Journal of the Acoustical Society of America, **110**, no. 6, 3011–3017, https://doi.org/10.1121/1.1417528.

Lu, Y., L. Stehly, R. Brossier, A. Paul, and AlpArray Working Group, 2020, Imaging Alpine crust using ambient noise wave-equation tomography: Geophysical Journal International, **222**, no. 1, 69–85, https://doi.org/10.1093/gji/ggaa145.

Merritt, M., G. Baeten, V. Rambaran, K. Godfrey, K. Bianchini, T. Brothers, F. Chelminski, et al., 2024, Revealing the subsalt in Garden Banks with a sparsely-shot TPS OBN and FWI: Fourth International Meeting for Applied Geoscience & Energy, SEG/AAGP, Expanded Abstracts, 958–962, https://doi.org/10.1190/image2024-4099710.1.
Mordret, A., M. Landès, N. M. Shapiro, S. C. Singh, P. Roux, and O. I. Barkved, 2013, Near-surface study at the Valhall oil field from ambient noise surface wave tomography: Geophysical Journal International, **193**, no. 3, 1627–1643, https://doi.org/10.1093/gji/ggt061.
Nouibat, A., R. Brossier, L. Stehly, J. Cao, A. Paul, Cifalps Team, and AlpArray Working Group, 2023, Ambient-noise wave-equation tomography of the Alps and Ligurian-Provence Basin: Journal of Geophysical Research: Solid Earth, **128**, no. 10, e2023JB026776, https://doi.org/10.1029/2023JB026776.
Nouibat, A., L. Stehly, A. Paul, S. Schwartz, T. Bodin, T. Dumont, Y. Rolland, R. Brossier, Cifalps Team, and AlpArray Working Group, 2022a, Lithospheric transdimensional ambient-noise tomography of W-Europe: Implications for crustal-scale geometry of the W-Alps: Geophysical Journal International, **229**, no. 2, 862–879, https://doi.org/10.1093/gji/ggab520.
Nouibat, A., L. Stehly, A. Paul, S. Schwartz, Y. Rolland, T. Dumont, W. C. Crawford, R. Brossier, Cifalps Team, and AlpArray Working Group, 2022b, Ambient-noise tomography of the Ligurian-Provence Basin using the AlpArray onshore-offshore network: Insights for the oceanic domain structure: Journal of Geophysical Research: Solid Earth, **127**, no. 8, e2022JB024228, https://doi.org/10.1029/2022JB024228.
Operto, S., Y. Gholami, V. Prieux, A. Ribodetti, R. Brossier, L. Métivier, and J. Virieux, 2013, A guided tour of multiparameter full waveform inversion for multicomponent data: From theory to practice: The Leading Edge, **32**, no. 9, 1040–1054, https://doi.org/10.1190/tle32091040.1.
Paul, A., M. G. Malusà, S. Solarino, S. Salimbeni, E. Eva, A. Nouibat, S. Pondrelli, et al., 2022, Along-strike variations in the fossil subduction zone of the western Alps revealed by the CIFALPS seismic experiments and their implications for exhumation of (ultra-) high-pressure rocks: Earth and Planetary Science Letters, **598**, 117843, https://doi.org/10.1016/j.epsl.2022.117843.
Provenzano, G., G. Bie'vre, R. Brossier, S. Garambois, and L. Métivier, 2024, Towards wave-equation ambient noise tomography of a landslide: The Harmalière case study: Fourth International Meeting for Applied Geoscience & Energy, SEG/AAPG, Expanded Abstracts, 1632–1636, https://doi.org/10.1190/image2024-4100725.1.
Rickett, J., and J. Claerbout, 1999, Acoustic daylight imaging via spectral factorization: Helioseismology and reservoir monitoring: The Leading Edge, **18**, no. 8, 957–960, https://doi.org/10.1190/1.1438420.
Rivera, C. A., P.-T. Trinh, E. Bergounioux, and B. Duquet, 2019, Elastic multiparameter FWI in sharp contrast medium: 89th Annual International Meeting, SEG, Expanded Abstracts, 1410–1414, https://doi.org/10.1190/segam2019-3215092.1.
Sambolian, S., R. Brossier, and L. Métivier, 2022, Exploiting the richness of multicomponent data: A time-dependent polarization-based FWI approach: 83rd Annual Conference and Exhibition, EAGE, Extended Abstracts, https://doi.org/10.3997/2214-4609.202210482.
Schuster, D., R. Brossier, L. Métivier, and A. Tarayoun, 2024, On the efficient use of HPC resources: Disaggregation of the full waveform inversion algorithm: 85th Annual Conference and Exhibition, EAGE.
Schuster, G. T., J. Yu, J. Sheng, and J. Rickett, 2004, Interferometric/daylight seismic imaging: Geophysical Journal International, **157**, no. 2, 838–852, https://doi.org/10.1111/j.1365-246X.2004.02251.x.
Sirgue, L., O. I. Barkved, J. Dellinger, J. Etgen, U. Albertin, and J. H. Kommedal, 2010, Full waveform inversion: The next leap forward in imaging at Valhall: First Break, **28**, no. 4, 65–70, https://doi.org/10.3997/1365-2397.2010012.
Spada, M., I. Bianchi, E. Kissling, N. P. Agostinetti, and S. Wiemer, 2013, Combining controlled-source seismology and receiver function information to derive 3-D Moho topography for Italy: Geophysical Journal International, **194**, no. 2, 1050–1068, https://doi.org/10.1093/gji/ggt148.
Tape, C., Q. Liu, A. Maggi, and J. Tromp, 2010, Seismic tomography of the Southern California crust based on spectral-element and adjoint methods: Geophysical Journal International, **180**, no. 1, 433–462, https://doi.org/10.1111/j.1365-246X.2009.04429.x.
Tarantola, A., 1984, Inversion of seismic reflection data in the acoustic approximation: Geophysics, **49**, no. 8, 1259–1266, https://doi.org/10.1190/1.1441754.
Wapenaar, K., 2003, Synthesis of an inhomogeneous medium from its acoustic transmission response: Geophysics, **68**, no. 5, 1756–1759, https://doi.org/10.1190/1.1620649.
Wapenaar, K., 2004, Retrieving the elastodynamic green's function of an arbitrary inhomogeneous medium by cross correlation: Physical Review Letters, **93**, 254301, https://doi.org/10.1103/PhysRevLett.93.254301.
Yang, P., R. Brossier, L. Métivier, and J. Virieux, 2016, A review on the systematic formulation of 3-D multiparameter full waveform inversion in viscoelastic medium: Geophysical Journal International, **207**, no. 1, 129–149, https://doi.org/10.1093/gji/ggw262.
Yong, P., R. Brossier, and L. Métivier, 2022, Parsimonious truncated Newton method for time-domain full-waveform inversion based on the Fourier-domain full-scattered-field approximation: Geophysics, **87**, no. 1, R123–R146, https://doi.org/10.1190/geo2021-0164.1.
Zhao, L., A. Paul, S. Guillot, S. Solarino, M. G. Malusà, T. Zheng, C. Aubert, et al., 2015, First seismic evidence for continental subduction beneath the western Alps: Geology, **43**, no. 9, 815–818, https://doi.org/10.1130/G36833.1.